Research Article | Vol. 29, No. 2 / 18 January 2021 / Optics Express 2819
Optics EXPRESS

Beam stability of buried-heterostructure quantum cascade lasers employing HVPE regrowth

JAE HA RYU,[1] JEREMY D. KIRCH,[1] BENJAMIN KNIPFER,[1] ZERUI LIU,[1] MORGAN TURVILLE-HEITZ,[2] TOM EARLES,[2] ROBERT A. MARSLAND,[2] AXEL STRÖMBERG,[3] GIRIPRASANTH OMANAKUTTAN,[3] YAN-TING SUN,[3] SEBASTIAN LOURDUDOSS,[3] DAN BOTEZ,[1] AND LUKE J. MAWST[1,*]

[1]*Department of Electrical and Computer Engineering, University of Wisconsin-Madison, 1415 Engineering Dr., Madison, WI 53706, USA*
[2]*Intraband, LLC, 200 N. Prospect Ave., Madison, WI 53726, USA*
[3]*Department of Applied Physics, KTH-Royal Institute of Technology, 106 91 Stockholm, Sweden*
[*]*mawst@engr.wisc.edu*

Abstract: Measurements of beam stability for mid-infrared (IR)-emitting quantum cascade lasers (QCLs) are important for applications that require the beam to travel through air to remote targets, such as free-space communication links. We report beam-quality measurement results of narrow-ridge, 4.6 µm-emitting buried-heterostructure (BH) QCLs fabricated using ICP etching and HVPE regrowth. Beam-quality measurements under QCW operation exhibit $M^2 < 1.2$ up to 1 W for ~5 µm-wide ridges. 5 µm-wide devices display some small degree of centroid motion with increasing output power (< 0.125 mrad), which corresponds to a targeting error of ~1.25 cm over a distance of 100 m.

1. Introduction

Semiconductor quantum cascade lasers (QCLs) emitting in the mid-infrared (IR) (λ = 3-5 µm) range are used for a wide range of applications such as remote sensing, free-space communications, infrared countermeasures and LIDAR. Scaling the power, while maintaining good beam quality, remains a challenging objective for mid-IR QCLs. QCLs exhibit a maximum operating current density (J_{max}) which is dependent on the injector doping level, but is typically in the range of 4-5 × the threshold-current density, J_{th}, value. Thus, since the power scales with the number of stages, N_s, the maximum output power at J_{max} is ultimately limited by the (active) core-region volume, defined by the product of N_s x the stage thickness and the pumped-region area. Longer cavity length can be used to scale the area, although internal losses generally limit the practical cavity lengths that can be used without incurring a significant reduction in slope efficiency. The number of core-region stages can be increased for large optical gain, but it is constrained by thermal-conductance considerations. Increasing the emitter width is limited as it decreases the effectiveness of heat removal in QCW/CW operation, and also leads to multi-spatial-mode operation. Multi-spatial-mode operation causes degraded beam quality and beam steering [1–3]. There have been methods reported to address this issue, such as using optical feedback, [4] but this requires additional optical components, which is not ideal. Another attractive approach for scaling the power while maintaining good beam quality would be to use phase-locked laser arrays of antiguides [5,6] which utilize global coupling [7] between the array elements for achieving both an uniform near-field intensity profile and stability against coupling-induced instabilities [8].

While many studies and experimental demonstrations were reported for phase-locked QCL arrays [9,10], little has been reported on the beam stability properties for both single-element

#414489 https://doi.org/10.1364/OE.414489
Journal © 2021 Received 10 Nov 2020; revised 23 Dec 2020; accepted 4 Jan 2021; published 15 Jan 2021

Optics EXPRESS

devices and phase-locked arrays, which is important for applications requiring long-range pointing accuracy, such as free-space communication links. Here we report beam-stability measurement results on single-element, 4.6 μm-emitting narrow-ridge buried-heterostructure (BH) QCLs grown by metalorganic chemical vapor deposition (MOCVD) and employing hydride vapor phase epitaxy (HVPE) for the semi-insulating (SI) InP:Fe regrowth. The HVPE process is attractive for selective regrowth, since high growth rates (0.2-0.3 μm/min) around 9-14 μm deep-etched ridges can be utilized and highly planar top surfaces can be readily obtained [11]. By contrast, MOCVD selective regrowth generally presents challenges to achieving top-surface planarity, and relatively long growth times are required [12]. HVPE regrowth has been previously employed for BH devices of MBE-grown QCL ridges [11], but beam-stability measurements were not reported [11]. Here we report a detailed study on the beam properties of collimated narrow-ridge BH QCLs under quasi-continuous wave (QCW) operation. The M^2 values, along with angular deviation of the beam as a function of drive current are reported for devices of two different ridge widths.

2. Device fabrication

A 40-stage, 4.6 μm-emitting step-tapered active-region (STA) QCL structure [13], with a 3 μm-thick n:InP (n~2×10^{16} cm^{-3}) upper-cladding layer and 1 μm-thick n+-doped (2×10^{19} cm^{-3}) InP contact layer was grown by MOCVD. Deep ridges aligned along [011], were formed using ICP etching, followed by brief HBr-based wet-chemical etching to clean the ICP-induced damage. Curved, wet-etched sidewalls with a trapezoidal active-region geometry are known to have higher thresholds than vertical sidewalls for ridge-guides [14] especially with narrow ridge widths, but we have found from COMSOL simulations that this effect is very much reduced for buried heterostructures. This is expected since, unlike in ridge-guide devices, BH devices do not have plasmon modes to couple to at the buried-ridge sidewalls. Nonetheless, ICP etching and vertical sidewalls are advantageous for narrow-ridge devices due to its ease of fabrication and efficient current injection.

InP:Fe was preferentially regrown in the field regions, using the SiO_2 mask employed for ridge etching, using HVPE. The regrowth was performed at the reactor pressure of 20 mbar and the growth temperature of 610°C. InCl and PH_3 were used as the group III and V precursors, respectively with V/III ratio of 7. The InCl was formed in situ by flowing HCl over the molten indium in a separately heated reactor zone. Ferrocene with a partial pressure of 1.4×10^{-5} mbar was used as the Fe dopant. A mixture of 5% H_2 in N_2 was used as the growth ambient, keeping the total gas flow through the reactor at 900 sccm. The growth conditions were selected based on previous experiments where effective current blocking and suppression of sidewall-ridge leakage was achieved [11]. The growth times of 26 and 32 minutes were used with different etch depths of QCL ridges aiming for planarized regrowth.

Single-emitter, edge-emitting QCLs operating in the important 4.5-5.0 μm wavelength region generally require a relatively narrow buried-ridge width (~ 5 μm) to maintain a single spatial mode under QCW/CW operating conditions. Two different samples of the same QCL material were processed with different ridge widths – while the ridge widths are not perfectly uniform throughout the sample, due to the HBr-based wet etch not etching evenly throughout the sample, on average the ridge width for one batch (Batch #1) was ~ 4 μm and for another (Batch #2) it was ~ 5 μm. As can be seen from the cross-sectional SEM image of a representative BH device from Batch #2 (~ 5 μm width) after the HVPE regrowth [Fig. 1(a)], the ridges were etched down to below the active region, and the HVPE regrowth resulted in a slightly overgrown but very well planarized structure [Fig. 1(b)]. In MOCVD-regrown BH devices, “rabbit ear” formation [15] can be observed depending on the processing steps or the shape of the ridge. Changes in the processing steps may be required to prevent or remove (by polishing) the “rabbit ears” depending on how severe the overgrowth, although the HVPE regrowth is largely independent

Optics EXPRESS

of such factors. The regrowth for the 4 µm-wide device was slightly less planar with a thinner regrown layer, but otherwise resulted in a similar geometry.

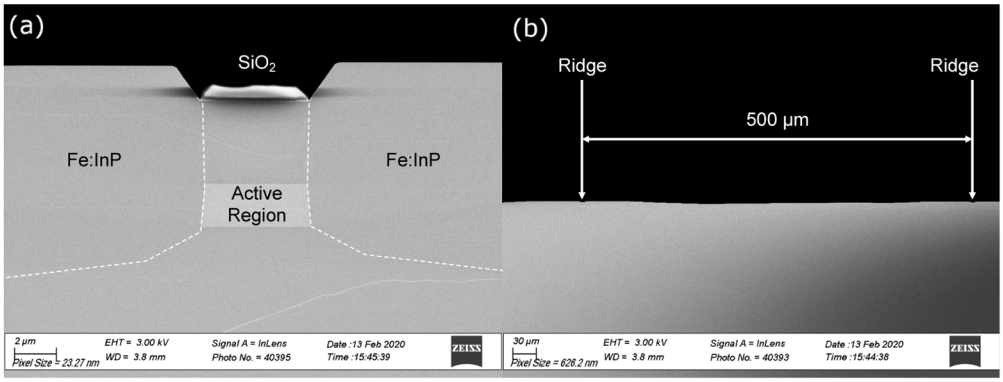

Fig. 1. SEM cross-section image after HVPE regrowth at (a) high magnification and (b) low magnification.

After the regrowth, the SiO_2 mask was removed and a 150 nm-thick Si_3N_4 film was deposited and patterned to provide current confinement. Subsequently, 20 nm Ti, 30 nm Pt, and 250 nm of Au were deposited by e-beam evaporation for the epi-side electrical contact. The wafer was then lapped and metallized by depositing 100 nm AuGe, 25 nm Ni, and 150 nm Au on the substrate side. Finally, 7.5 mm-long bars were cleaved and high-reflectivity (HR)-coated on the rear facet with an uncoated (UC) front (emitting) facet, followed by chip separation. Laser chips were then mounted in the epi-side down configuration with indium solder on CuW heatsinks.

3. Beam-stability measurement results

All measurements were carried out with the measurement-stage temperature maintained at 20°C. Figure 2(a) shows the light-current-voltage (L-I-V) data of representative BH devices from batches #1 and #2 and also an HR-coated/UC ridge-guide device of the same length (width ~ 22.1 µm at the center of the active region) in short-pulse operation (200 ns-wide pulses, 20 kHz rep. rate). The devices were from the same QCL material, for comparison purposes, and Fig. 2(b) shows cross-sectional SEM images of BH devices where the epi-side is at the bottom of the images. It should be noted that the thickness of the regrown layers are different for these devices (4 µm device has thinner regrowth), but we verified through COMSOL simulations that this difference in regrowth thickness has no effect on the optical properties. Table 1 summarizes the maximum peak output power (P_{max}), threshold-current density (J_{th}), slope efficiency (η_s), and peak wall-plug efficiency (WPE) of the devices. The maximum output power of the ridge-guide was ~6.2-6.9 W, compared to ~1.79 W for the 4 µm-wide BH device. The ridge-guide has roughly 5 times the volume of the 4 µm BH device, while the output power only scales by ~3.4-3.8 – we believe this may be due to the sloped sidewalls of the ridge-guide active region, as the trapezoidal geometry leads to wasted current and lower injection efficiency. The J_{th} value was ~ 1.01–1.12 kA/cm^2, and the η_s value was ~ 2.53–2.55 W/A. The J_{th} value of the ridge-guide devices is close to the J_{th} value of the 5 µm-wide, 7.5 mm-long BH device (1.08 kA/cm^2) as expected, since the waveguide loss coefficient α_{w} of ~ 20 µm-wide ridge-guide devices is generally found to be quite similar to that of BH devices [16]. Further proof that the α_{w} value of the ridge-guide devices is similar to that of BH devices is that their η_s values, for the same cavity length, are basically the same. It should be noted, as seen in Table 1, that the threshold-current density is higher and the slope efficiency is lower for the 4 µm-wide device compared to the other devices. While rough sidewalls can result in significant scattering losses for ridge-guide devices [17], such scattering losses are

Optics EXPRESS

expected to be less of an issue for buried heterostructures [18] (as the regrown layers passivate the sidewalls and reduce the index difference at the sidewalls). We believe that the higher J_{th} may originate from the higher optical field overlap with the regrowth interface and the Fe:InP regrown material for the narrower-width device, perhaps leading to increased optical losses and/or an increased amount of sidewall current leakage for the narrow-ridge device. Further studies regarding the dependence of J_{th} on ridge width are required to fully understand this observed behavior.

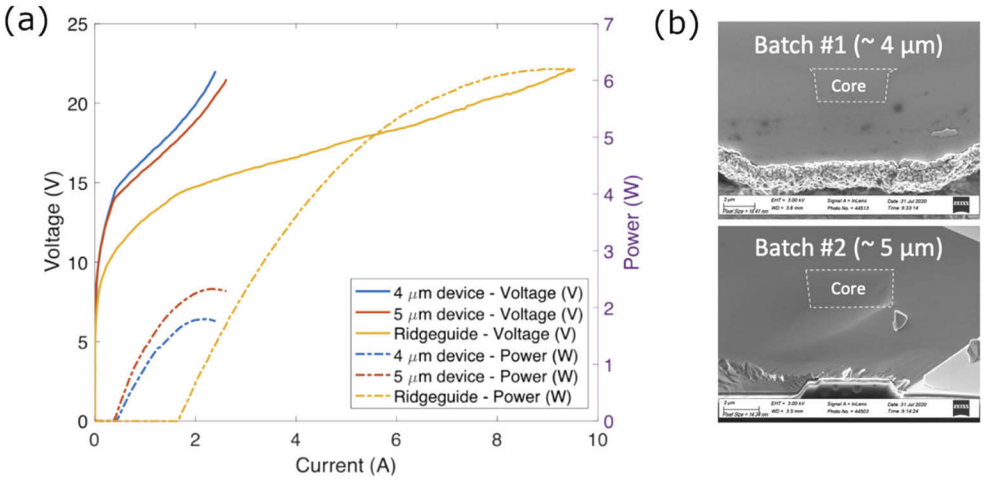

Fig. 2. (a) Measured L-I-V data for ~4 µm- and ~5 µm-wide BH devices and a ~22.1 µm-wide ridgeguide (L = 7.5 mm) under short-pulse (200 ns-wide pulse, 20 kHz rep. rate) conditions, and (b) SEM cross-section images of the BH devices.

Table 1. Summary of device characteristics – maximum pulsed output power (P_{max}), threshold current density (J_{th}), slope efficiency (η_s), and wallplug efficiency (WPE)

Device	P_{max} (W)	J_{th} (kA/cm2)	η_s (W/A)	WPE (%)
4 µm BH	1.79	1.33	1.86	5.9
5 µm BH	2.33	1.08	2.42	8.2
Ridgeguide	6.20 (L = 7.5 mm)	1.12 (L = 7.5 mm)	2.55 (L = 7.5 mm)	6.8 (L = 7.5 mm)

The L-I-V and M^2 values were also measured and calculated with 100-µs pulses, under QCW operation. The M^2 factor, or the beam quality factor, is a common method to quantify the beam quality. The beam quality factor along the lateral direction (M_x^2) is calculated by the following formula: $M_x^2 = \frac{\pi}{\lambda}\frac{d_{\sigma x0}\Theta_{\sigma x0}}{4}$ where $d_{\sigma x}$ is the beam waist width, and $\Theta_{\sigma x}$ is the far-field beam divergence angle [19]. We have not included the M^2 along the y-direction (transverse), as the narrow aperture (~ 2 µm) ensures single-spatial-mode operation. The beam waist width and far-field beam divergence angle are found using a camera that consists of 160 × 160 pixels. The camera is first moved along the collimated beam after the ~ 1-mm focal length, high-NA collimating lens to find the position of the beam waist, and the beam waist width is found from the second-order moment of the power-density distribution, which is also known as the four-sigma width. The far-field divergence angle is then found by placing the camera at the focal plane of a focusing mirror, where $\Theta_{\sigma x}$ is found by dividing the four-sigma beam width at the focal plane by the focal length of the mirror. The focusing mirror is approximately 1-m after the collimating lens and produces the collimated-beam far-field pattern at the camera plane. Figure 3 shows the device characteristics after beam collimation, measured under QCW operation (100 µsec pulse

Optics EXPRESS

width, 0.5%−10% duty cycle): (a) L-I-V curves, and (b) output-power dependent M^2 values along the lateral direction. Very good beam quality factors, $M^2 < 1.2$, are observed for both ridge widths, but, as shown below, the narrower ridge exhibits better pointing stability.

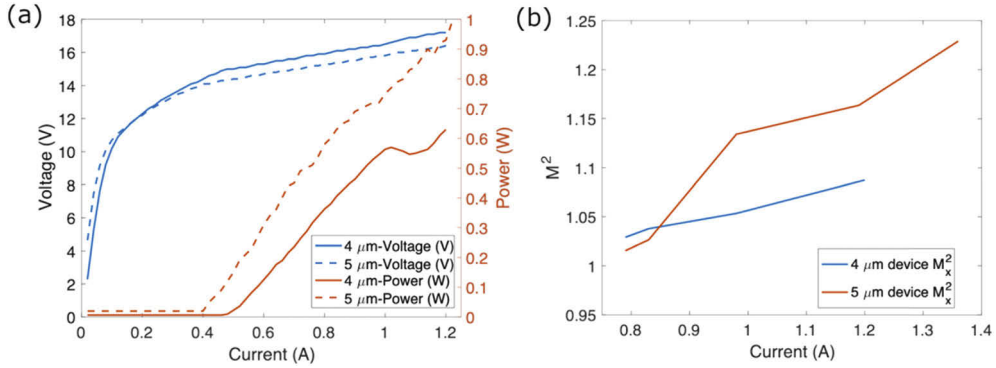

Fig. 3. (a) Measured L-I-V characteristics and (b) M^2 along x-direction (lateral) under QCW operation for the 4- and 5-μm-wide BH devices after beam collimation.

The beam stability of these devices was investigated by measuring the angular deviations of the far-field beam patterns at different output powers using the same setup as for the divergence-angle measurement. The angular deviation is found by first subtracting the centroid location (in microns) by the mean value, to get the deviation, which is then divided by the focal length of the focusing mirror (2032 mm) to convert into the angle in mrad. This measurement of the angular deviation of the collimated beam provides a more sensitive measure of beam deviation compared to using the change in beam waist width, and is also more meaningful when considering applications requiring beam stability over long distances in free space. Figure 4 shows the angular deviations of their far-field beam patterns as a function of output power under QCW (100 μsec pulse width, 0.5% duty cycle) operation taken over time on the same device. Devices with wider ridge width from batch #2 (~5 μm-wide buried ridge) display some small degree of centroid motion with increasing output power (< 0.125 mrad) [Fig. 4(a)], which corresponds to a targeting error of ~1.25 cm over a distance of 100 m. This is a large improvement compared to previously reported results where the beam steered by ~ 2-3° for an 8 μm-wide BH [3]. We can see the beam is stable along the y-direction for both devices, which is expected, as higher-order modes are cut-off in that direction. Significantly improved lateral-beam stability is observed for devices with narrower ridge width [Fig. 4(b)], up to a kink-point in the L-I curve (~ 0.55 W), although at the expense of reduced output power. This kink is likely due to a thermally induced instability, which leads to optical-mode beam steering. That is, it is possible, under quasi-CW driving conditions, that current crowding occurs to one side of the buried ridge because of a hot spot at a defect at the regrown interface. Then the gain profile is distorted, which would cause the phase to change across the buried ridge and result in beam steering. We noticed that for the 5 μm-wide device the kinks in the L-I curve [Fig. 3(a)] are not as severe as for the 4 μm-wide device, even though it shows a higher degree of centroid motion. That same current-crowding effect may also be the cause of the temporary power drop (i.e., the pronounced kink for the 4 μm-wide device) due to a temporary current redistribution in and/or around the buried ridge.

Optical simulations were performed to better understand how the device geometry affects the performance. The 4 μm and 5 μm-wide BH devices described earlier were imaged by SEM and modeled in COMSOL Multiphysics to take into account the geometry (curvatures of regrowth, active-region shape and width, etc), as shown in Fig. 5. The HVPE regrowth resulted in a very well planarized structure, where for the 4 μm-wide device [Fig. 5(a)] it was slightly less

Optics EXPRESS

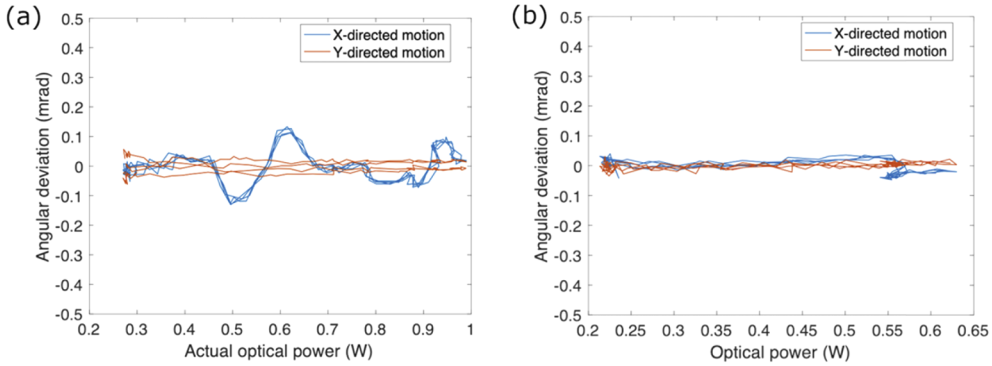

Fig. 4. Measured angular deviation of the collimated-beam far-field centroid position along x- (lateral) and y- (transverse) directions, as a function of output power under QCW operation for (a) ~5 µm-wide ridge device and b) ~4 µm-wide ridge device.

planar with a thinner regrown layer, while for the 5 µm-wide device the Fe:InP layer was slightly overgrown.

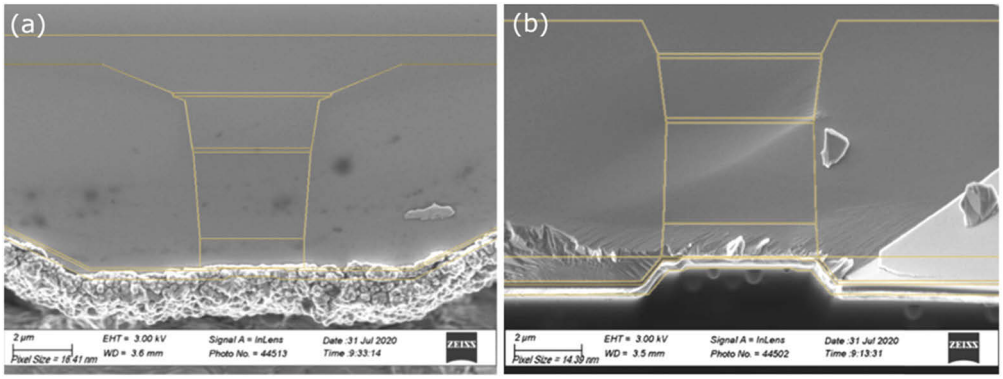

Fig. 5. SEM cross-section of the (a) ~4 µm-wide BH device and (b) ~ 5 µm-wide BH device

Supported lateral optical modes were found using COMSOL Multiphysics, and initial results are summarized in Table 2 below. The actual device geometries, shown by the yellow outlines indicated in Fig. 5, were used in the COMSOL model to simulate the threshold gain values for the fundamental and first-order spatial modes. The refractive index values used in the COMSOL model are indicated in Table 3. The core region refractive index is averaged across the thin layers assuming a TM mode [20]. The refractive index values of the metals (Au, Cu and Ti) are taken from previous measurements [21–23], while the other values are estimated using a Drude model with material parameters taken from the Ioffe Ref. [24].

The modal loss is found by $\alpha_{Comsol} = \frac{4\pi}{\lambda} Im(n_{eff})$, and the TM confinement factor is found by $\Gamma = \int_{Core} |E_y|^2 / \int_{all} |\boldsymbol{E}|^2$ – it should be noted that the loss found by COMSOL does not take into account intersubband (ISB) absorption losses [16]. Using these values, the threshold gain of each mode for both devices were calculated. The threshold gain was calculated using the following formula: $g_{th} = \frac{\alpha_{Comsol} + \alpha_m}{\Gamma}$, where α_m is the mirror loss. Note that both device widths support fundamental and first-order modes, and the modal losses are similar for both modes. In this case, intermodal discrimination is provided by the difference in optical confinement factors. From the threshold gain values, we can see that the difference in threshold gain between the

Optics EXPRESS

Table 2. Simulated modal loss and confinement factor and its calculated threshold gain for the 4 µm- and 5 µm-wide BH devices

Device	Type of Mode	n_{eff}	Modal Loss (cm^{-1})	Confinement Factor (Γ)	Threshold Gain g_{th} (cm^{-1})
Narrow active region BH (~ 4 µm)	Fundamental Mode	3.1814-3.7373E-5i	1.04	67.80%	2.99
	First-order Mode	3.1223-3.1326E-5i	0.87	49.62%	3.75
Wide active region BH (~ 5 µm)	Fundamental Mode	3.1824-3.2185E-5i	1.04	68.05%	2.99
	First-order Mode	3.1265-3.2185E-5i	0.89	52.73%	3.58

Table 3. The refractive index values used in the COMSOL model for the 4 µm and 5 µm-wide BH devices

Material	Refractive Index
2 x 10^{19} InP	2.20124+0.026416i
4 x 10^{17} InP	3.08459+0.000377i
2 x 10^{16} InP	3.09923+1.87625E-5i
Fe:InP	3.09997+6.34895E-8i
5 x 10^{16} InGaAs	3.40881+7.88405E-5i
Active Region	3.26002+4.01336E-5i
Si_3N_4	1.3583+0.00065167i
Ti	2.74607+8.00431i
Gold	2.94474+33.1992i

fundamental mode and the first-order mode is larger for the narrower device, which helps suppress the onset of lasing in the first-order mode in that case. However, gain-spatial-hole burning above laser threshold may lead to the onset of lasing for the first-order lateral mode, particularly if the threshold gain difference between the fundamental and first-order mode is small. Multimode operation has been shown to lead to mode instabilities, including beam steering [1–3], and the wider active-region device is more likely to support lasing in both the fundamental and first-order spatial mode, which could explain the reduced pointing stability compared with the narrower active-region device. Further narrowing of the device width to ~3 µm, would result in cut-off of the first-order mode, although the maximum output powers would be further reduced. An above-threshold model which includes gain-spatial-hole burning and thermal lensing would be required to simulate these devices more accurately.

4. Conclusion

We have presented beam-stability measurement results on narrow-ridge QCL BH devices, where the semi-insulating InP layers were selectively regrown using HVPE, resulting in a well-planarized surface. M^2 factors and the angular deviation of the far-field beam at different output powers were measured for devices of two different ridge widths – good M^2 factors (< 1.2) were measured for both devices, while the narrow device displayed better lateral beam stability, at the expense of output power. Optical simulations indicate that for the wider ridge device, multimode operation is likely a result of a lower threshold gain for the first-order mode, which may well lead to the observed beam steering and pointing instabilities. These results on a single-emitter QCL help elucidate the sensitivity of pointing stability on device aperture width. Further coherent output power scaling of QCLs, while maintaining beam stability, may be possible by on-chip phase-locking of narrow-element-width arrays.

Funding. Air Force Office of Scientific Research (FA9550-19-1-0385); Vetenskapsrådet (2015-05470); Horizon 2020 Framework Programme (828893).

Disclosures. The authors declare no conflicts of interest.

References

Optics EXPRESS

1. N. Yu, L. Diehl, E. Cubukcu, D. Bour, S. Corzine, G. Höfler, A. K. Wojcik, K. B. Crozier, A. Belyanin, and F. Capasso, "Coherent Coupling of Multiple Transverse Modes in Quantum Cascade Lasers," Phys. Rev. Lett. **102**(1), 013901 (2009).
2. W. W. Bewley, J. R. Lindle, C. S. Kim, I. Vurgaftman, J. R. Meyer, A. J. Evans, J. S. Yu, S. Slivken, and M. Razeghi, "Beam steering in high-power CW quantum-cascade lasers," IEEE J. Quantum Electron. **41**(6), 833–841 (2005).
3. Y. Bai, N. Bandyopadhyay, S. Tsao, E. Selcuk, S. Slivken, and M. Razeghi, "Highly temperature insensitive quantum cascade lasers," Appl. Phys. Lett. **97**(25), 251104 (2010).
4. L. Jumpertz, S. Ferré, M. Carras, and F. Grillot, "Beam steering in quantum cascade lasers with optical feedback," Proc. SPIE **10111**, 101112F (2017).
5. D. Botez, L. J. Mawst, and G. Peterson, "Resonant leaky-wave coupling in linear arrays of antiguides," Electron. Lett. **24**(21), 1328–1330 (1988).
6. D. Botez, L. J. Mawst, G. L. Peterson, and T. J. Roth, "Phase-locked arrays of antiguides: modal content and discrimination," IEEE J. Quantum Electron. **26**(3), 482–495 (1990).
7. W. J. Fader and G. E. Palma, "Normal modes of N coupled lasers," Opt. Lett. **10**(8), 381–383 (1985).
8. R. D. Li and T. Erneux, "Stability conditions for coupled lasers: series coupling versus parallel coupling," Opt. Commun. **99**(3-4), 196–200 (1993).
9. J. D. Kirch, C. C. Chang, C. Boyle, L. J. Mawst, D. Lindberg III, T. Earles, and D. Botez, "5.5 W near-diffraction-limited power from resonant leaky-wave coupled phase-locked arrays of quantum cascade lasers," Appl. Phys. Lett. **106**(6), 061113 (2015).
10. C. Sigler, R. Gibson, J. H. Ryu, C. A. Boyle, J. D. Kirch, D. Lindberg III, T. Earles, D. Botez, L. J. Mawst, and R. Bedford, "5.3 μm-Emitting Diffraction-Limited Leaky-Wave-Coupled Quantum Cascade Laser Phase-Locked Array," IEEE J. Sel. Top. Quantum Electron. **25**(6), 1–9 (2019).
11. W. Metaferia, B. Simozrag, C. Junesand, Y. T. Sun, M. Carras, R. Blanchard, F. Capasso, and S. Lourdudoss, "Demonstration of a quick process to achieve buried heterostructure quantum cascade laser leading to high power and wall plug efficiency," Opt. Eng. **53**(8), 087104 (2014).
12. L. Cheng, J. Fan, D. Janssen, D. Guo, X. Chen, F. J. Towner, and F. S. Choa, "Analysis of InP regrowth on deep-etched mesas and structural characterization for buried-heterostructure quantum cascade lasers," J. Electron. Mater. **41**(3), 506–513 (2012).
13. D. Botez, J. D. Kirch, C. Boyle, K. M. Oresick, C. Sigler, H. Kim, B. Knipfer, J. H. Ryu, D. Lindberg III, T. Earles, and L. J. Mawst, "High-efficiency, high-power mid-infrared quantum cascade lasers," Opt. Mater. Express **8**(5), 1378–1398 (2018).
14. X. Huang, Y. Chiu, W. O. Charles, and C. Gmachl, "Ridge-width dependence of the threshold of long wavelength ($\lambda \approx 14$ μm) quantum cascade lasers with sloped and vertical sidewalls," Opt. Express **20**(3), 2539 (2012).
15. B.-T. Lee, R. A. Logan, and S. N. G. Chu, "Observation of growth patterns during atmospheric pressure metalorganic vapor phase epitaxy regrowth of InP around etched mesas," J. Cryst. Growth **130**(1-2), 287–294 (1993).
16. D. Botez, C. C. Chang, and L. J. Mawst, "Temperature sensitivity of the electro-optical characteristics for mid-infrared ($\lambda = 3$–16 μm)-emitting quantum cascade lasers," J. Phys. D: Appl. Phys. **49**(4), 043001 (2016).
17. F. Toor, D. L. Sivco, H. E. Liu, and C. F. Gmachl, "Effect of waveguide sidewall roughness on the threshold current density and slope efficiency of quantum cascade lasers," Appl. Phys. Lett. **93**(3), 031104 (2008).
18. C. Ji, R. G. Broeke, Y. Du, J. Cao, N. Chubun, P. Bjeletich, F. Olsson, S. Lourdudoss, R. Welty, C. Reinhardt, P. L. Stephan, and S. J. B. Yoo, "Monolithically integrated InP-based photonic chip development for O-CDMA systems," IEEE J. Sel. Top. Quantum Electron. **11**(1), 66–77 (2005).
19. . "Lasers and laser-related equipment – Test methods for laser beam widths, divergence angles and beam propagation ratios – Part 1: Stigmatic and simple astigmatic beams," ISO 11146-1:2005(E).
20. D. E. Aspnes, "Optical Properties of Thin Films," Thin Solid Films **89**(3), 249–262 (1982).
21. M. A. Ordal, R. J. Bell, R. W. Alexander Jr., L. L. Long, and M. R. Querry, "Optical properties of Au, Ni, and Pb at submillimeter wavelengths," Appl. Opt. **26**(4), 744–752 (1987).
22. M. A. Ordal, R. J. Bell, R. W. Alexander Jr., L. L. Long, and M. R. Querry, "Optical properties of fourteen metals in the infrared and far infrared: Al, Co, Cu, Au, Fe, Pb, Mo, Ni, Pd,Pt, Ag, Ti, V, and W," Appl. Opt. **24**(24), 4493–4499 (1985).
23. M. A. Ordal, R. J. Bell, R. W. Alexander. Jr., L. A. Newquist, and M. R. Querry, "Optical properties of Al, Fe, Ti, Ta, W, and Mo at submillimeter wavelengths," Appl. Opt. **27**(6), 1203–1209 (1988).
24. Ioffe Institute, NSM Archive - Physical Properties of Semiconductors (http://www.ioffe.rssi.ru/SVA/NSM/Semicond)